UC Berkeley
UC Berkeley Previously Published Works

Title

Exceptional cryogenic-to-ambient impact toughness of a low carbon micro-alloyed steel with a multi-heterogeneous structure

Permalink

https://escholarship.org/uc/item/7zn914d5

Authors

Xu, Xiaoning

Kumar, Punit

Cao, Ruqing

et al.

Publication Date

2024-08-01

DOI

10.1016/j.actamat.2024.120019

Copyright Information

Peer reviewed
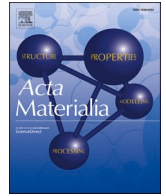
Full length article

Exceptional cryogenic-to-ambient impact toughness of a low carbon micro-alloyed steel with a multi-heterogeneous structure

Xiaoning Xu [a,1], Punit Kumar [b,c,1], Ruqing Cao [d], Qibin Ye [a], Yuexin Chu [a,e], Yong Tian [a,*], Yi Li [d,*], Robert O. Ritchie [b,c,*]

[a] State Key Laboratory of Rolling and Automation, Northeastern University, Shenyang, PR China
[b] Department of Materials Science and Engineering, University of California, Berkeley, CA, USA
[c] Materials Sciences Division, Lawrence Berkeley National Laboratory, Berkeley, CA, USA
[d] Shenyang National Laboratory for Materials Science, Institute of Metal Research, Chinese Academy of Sciences, Shenyang, PR China
[e] Institute of Materials Plainification, Liaoning Academy of Materials, 280 Chuangxin Road, Shenyang, PR China

ARTICLE INFO

ABSTRACT

A low-carbon micro-alloyed (LCMA) steel with a body-centered cubic (*bcc*) crystal structure suitable for extremely low temperatures was developed by overcoming the intrinsic ductile-to-brittle transition in *bcc* alloys at cryogenic temperatures. The excellent cryogenic-to-ambient impact toughness in the LCMA rolled plate results from its heterogeneous microstructure, which gradually changes from bamboo-like ultrafine grains (~ 1.1 μm) on the surface to relatively equiaxed coarse grains in the core (~ 3.4 μm), accompanied by a distinct texture gradient variation. The heterostructured LCMA steel displays a cryogenic impact toughness of $\sim$200 J/cm^2 at 77 K, which is 24 times higher than the coarse-grained LCMA steel. Such high impact toughness of heterostructured LCMA arises from the coordinated deformation mechanisms over different length-scales coupled with delamination toughening. At 77 K, the heterostructured steel plate deforms by forming cellular sub-structures at the core to the surface, which refines the microstructure and promotes hetero-deformation induced (HDI) hardening to improve intrinsic toughening. Moreover, the subsequent delamination process induces extrinsic toughening by shielding and blunting the cracks, with the local plane-stress conditions induced by delamination promoting ductile fracture of the coarse grains in the core regions. This low alloy steel with its heterogeneous microstructure exhibits extraordinary impact toughness at cryogenic temperatures highlights the possibility of materials design strategies for sustainable development.

1. Introduction

The development of high-strength structural steel with superior fracture resistance, suitable for safety-critical applications, remains a significant challenge. This is particularly pertinent for low alloy steels with body-centered cubic (*bcc*) structures, as they can lose substantial ductility and toughness below their ductile-to-brittle transition temperature (DBTT). The DBTT in steels can lead to sudden, catastrophic failures and potentially fatal accidents such as the Liberty ships failures, where the hull of ships fractured in cold water in the 1940s [1,2]. Owing to intensified demands for steel capable of operating at extremely low temperatures, methods for reducing the DBTT primarily have focused on high-volume alloying of steels – commonly with nickel (Ni) [3–5] and

manganese (Mn) [5,6]. These elements stabilize the austenite phase of face-centered cubic (*fcc*) structures, which maintains a relatively stable fracture mode at cryogenic temperatures. The stable fracture of *fcc* austenitic steels at cryogenic temperatures arises from extensive plastic deformation near the crack tip supported by the temperature insensitivity of dislocation movement compared to *bcc* materials [7]. However, the large-scale production and recycling processes of these austenitic steels are environmentally contentious and expensive, which raises questions about the sustainable economic viability of these alloys [8].

Another way to lower the DBTT of *bcc* steels is to refine the grain size, an approach that is in line with the concept of material "plainification", i.e., the improvement of mechanical properties by modifying the microstructural morphology rather than by the addition of large

---

* Corresponding authors.
E-mail addresses: tianyong@ral.neu.edu.cn (Y. Tian), liyi@imr.ac.cn (Y. Li), roritchie@lbl.gov, ritchie@berkeley.edu (R.O. Ritchie).
[1] These authors contributed equally to this work.

amounts of alloying elements [1,2,8–13]. By employing low-cost thermo-mechanical approaches such as warm rolling (WR) [9–11] and accumulative roll bonding (ARB) [12,13], high-strength ultra-fine grained (UFG, with grain sizes ≤ 1 μm) *bcc* steels have been designed. Regrettably, UFG steels, despite their desirable DBTT, show compromised ductility, toughness, and low work-hardening capabilities at ambient temperatures [9–13]. To achieve high strength with reduced DBTT, Kimura *et al.* combined grain refinement with delamination, by producing a bamboo-like ultrafine-grained low-carbon steel using a temp-formed process [2]. Despite these advances, this type of steel severely loses toughness when exposed to cryogenic temperatures (77 K). Further modifications by Sun et al. enhanced the laminated ultrafine grain structure by introducing a martensitic phase into the ferrite matrix, resulting in significant impact energy retention (~240 J) at liquid nitrogen temperatures [14]. However, a desirable impact toughness was only observed when cracks followed a specific "crack arrester" direction; other paths, such as the "crack divider," led to sharply reduced impact resistance [9,10,15]. The "crack divider" direction of the elongated UFG microstructure in steel plates often aligns with the transverse direction, which is frequently required in relevant standards for conducting impact toughness testing [16]. Also, an absence of typical ductile characteristics on the fracture surfaces, the lack of tensile ductility (which was only ~2 %), and poor fracture toughness (~8 MPa·m$^{1/2}$) at 77 K suggests that improvements in the plastic deformation ability of the ferritic/martensitic UFG structure are definitely required [14].

A recent innovative approach to solving this issue has involved incorporating heterogeneous microstructures into steels to synergistically improve material properties such as strength, ductility, and toughness by providing an alternative non-alloying pathway to enhance the strain hardening ability of ultrafine/nano metals [17–25]. Notable heterogeneous structures include gradient structures [17–22], bimodal structures [23], dual-phase structures [24], and heterogeneous lamellar structures [25]. Gradient-structured nickel shows high fracture resistance in different orientations, which is maintained under both quasi-static and dynamic loading without sacrificing strength, highlighting the potential of these approaches [21,22].

Considering these developments, here we investigate the prospect of utilizing low carbon micro-alloyed (LCMA) steels with heterogeneous structures to overcome the challenges of inherent brittleness in *bcc* steels at cryogenic temperatures. Accordingly, LCMA rolled steel plates developed with heterogeneous structures and their mechanical properties, including the dynamic impact toughness, were comprehensively investigated at various temperatures. The resulting mechanical properties and microstructure of this heterostructured (HS) LCMA steel are bench-marked against more conventional LCMA steels with traditional (nominally uniform) coarse-grained (CG) and ultrafine-grained microstructures (UFG).

2. Experimental procedures

2.1. Materials processing

The composition (in wt.%) of low carbon microalloyed steel is 0.05 % C, 0.15 % Si, 1.95 % Mn, 0.2 % Cr, 0.55 % Ni, 0.052 % Ti+Nb, and 0.035 % Al, with balanced Fe [26]. The equilibrium temperatures for the beginning and the end of phase transition from austenite to ferrite (A_{e3} and A_{e1}) were determined by Thermo-calc software (TCFE9 database) as 1087 and 937 K, respectively. The austenite phase is stable above A_{e3} and completely unstable below A_{e1}, therefore, completely transforms to ferrite in time [27].

Rectangular commercial cast ingots (100 × 80 × 120 mm^3, length × width × height) of LCMA steel were subjected to an austenitization process at 1473 K for 4 h. Subsequently, a rough rolling was applied to reduce the thickness from 120 to 85 mm using a 450-mm diameter two-high reversible and hot rolling mill. After austenitizing and rough rolling, the temperature was maintained at ~1323 K and carefully

monitored by a VF-3000 infrared radiation thermometer before three different processing routes were followed to achieve the distinct coarse-grained, ultrafine-grained and heterostructured (HS) microstructures:

(i) *Coarse-grained microstructure:* The CG microstructure was prepared by conventional thermo-mechanical processing (Fig. 1(a)). After the rough rolling, eight passes of finish rolling were applied to decrease the thickness from 85 to ~5 mm; during the process, the temperature of the CG plate dropped to ~1123 K from the initial ~1323 K. The plate was then cooled to a temperature of ~773 K by laminar cooling at a rate of ~23 K/s, followed by air cooling to ambient temperature.

(ii) *Ultrafine-grained microstructure*: A schematic of the process for the UFG microstructure is shown in Fig. 1(b). After initial rough rolling, the plate was water-quenched to ambient temperature before being reheated and held at a temperature of 983 K (in the austenite and ferrite dual-phase region) for 1.5 h to homogenize the microstructure. Subsequently, an 85 mm thick plate was warm rolled with eight passes to ~6 mm, followed by laminar cooling to ~673 K and then air cooling to ambient temperature. To compare the properties with other microstructures, the steel plate was mechanically machined to a 5 mm thickness.

(iii) *Heterostructured (HS) microstructure*: A schematic of the process for the heterostructured microstructure is shown in Figs. 1(c, d). After initial rough rolling, the plate was cooled at a cooling rate of ~50 K/s from 1323 to 673 K (surface temperature) using an ultra-fast cooling (UFC) facility [28]; this breaks up the steam film on the surface of the plate more effectively compared to the conventional laminar cooling and resulted in a large temperature gradient from the plate surface to its core [28,29]. The temperature gradient across the thickness of the steel plate was measured by thermocouples inserted in the mid-thickness and onto the top and bottom surfaces of the plate, which indicated a core temperature of ~1302 K at this time. The temperature difference indicates a gradient microstructure, i.e., a bainite/ferrite structure on the plate surface, which gradually transitioned to austenite near the core. The plate was subjected to rolling with 8 passes to reduce the thickness from 85 to ~5 mm. The surface temperature after the final rolling step was ~993 K (due to the heat transfer from the core to the surface). The plate was then cooled to ~673 K by laminar cooling, followed by air cooling to ambient temperature. In Fig. S1a, the RD, TD, and ND labels represent the rolling direction, transverse direction, and normal direction of the steel plates, respectively.

2.2. Microstructure characterization

The specimens were mechanically polished to a mirror finish and etched prior to microstructural characterization by scanning electron microscopy (SEM) in a ZEISS Crossbeam 550. The texture of the specimens was examined by electron backscattered diffraction (EBSD) using a Symmetry-EBSD detector at 15 kV and a step size of 50 nm. EBSD data were analyzed using commercially available software AZtecCrystal and HKL Channel 5 from Oxford Instruments. Transmission electron microscopy (TEM) was carried out on an FEI Talos 200X TEM microscope operating at 200 kV and equipped with a high-angle annular dark field (HAADF) detector. Fractography on the specimens was performed by confocal laser scanning microscopy (CLSM, Olympus LEXT OLS4000) to reconstruct the three-dimensional morphologies of the fracture surfaces.

2.3. Mechanical characterization

2.3.1. Uniaxial tensile testing

For tensile testing, the CG, UFG, and heterostructured plates were cut into dog-bone shaped samples of 70 mm in length, a gauge cross-section of 8 × 5 mm^2, and a gauge length of 30 mm along the RD (Fig. S1). The
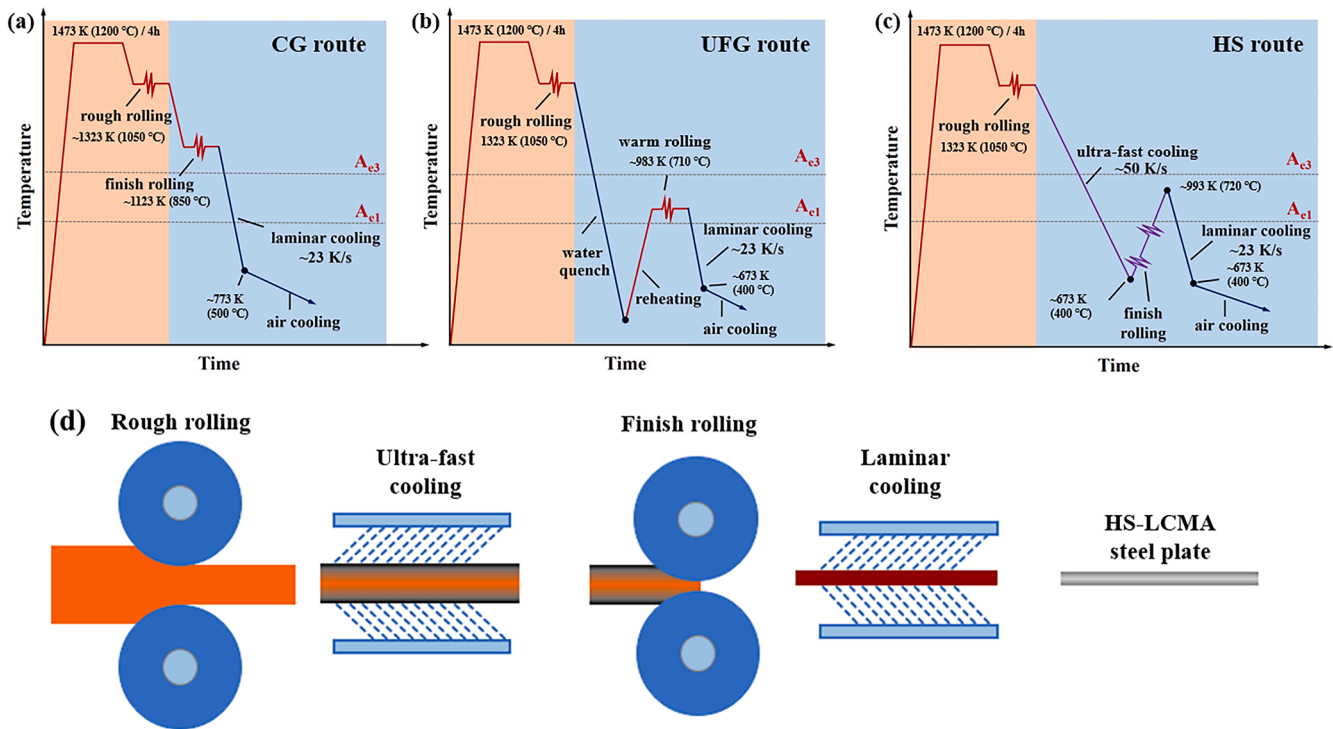
Fig. 1. Schematic diagram of the processing by rolling and cooling for the production of the (a) GG, (b) UFG, and (c-d) HS microstructures.

uniaxial quasi-static tensile tests at room (RT, 293 K) and liquid nitrogen (77 K) temperatures were performed at a strain rate of $1 \times 10^{-3}\,s^{-1}$. Two tensile tests were carried out for each microstructural condition.

2.3.2. Charpy impact testing

Rectangular Charpy impact samples of dimensions $5 \times 10 \times 55$ mm^3 were machined with length parallel to the rolling directions. A 45° V-notch, 2 mm in depth, was machined in the middle of the sample (Fig. S1). Impact energy vs. temperature curves were obtained by Charpy impact tests performed at temperatures from 293 K to 77 K using a SANS ZBC2452-B pendulum impact testing equipment. At least three measurements were performed for each condition to determine the average impact energy.

2.3.3. Instrumented Charpy impact testing

To shed light on the energy absorption during the various stages of fracture during impact toughness tests, instrumented Charpy pendulum impact testing was performed using MPX pendulum impact testers at 293 K and 77 K; this impact tester was capable of recording the dynamic load-displacement curves. The four different stages of fracture that can be analyzed, schematically illustrated in Fig. 2, are crack initiation, stable crack propagation, unstable crack propagation, and plastic collapse [21,30–32]. Akin to the quasi-static fracture toughness tests, the relationship between the fracture toughness (J) and crack length (Δa) of the impact specimens (pre-cracked) can be obtained at high loading rates from the recorded load-displacement curves [21,33,34]. For the notched impact specimens without fatigue pre-cracking, which were used in this study, the dynamic J-R curve can still be estimated using the "key curve" method [21,35,36], as described in the Supplementary Information. Since the nonlinear-elastic fracture-e-mechanics-based J-integral resistance curve (i.e., the J-R curve) is effective in characterizing the evolution of crack initiation and crack growth, the J-integral and J-R curves of different conditions were obtained for comparison.
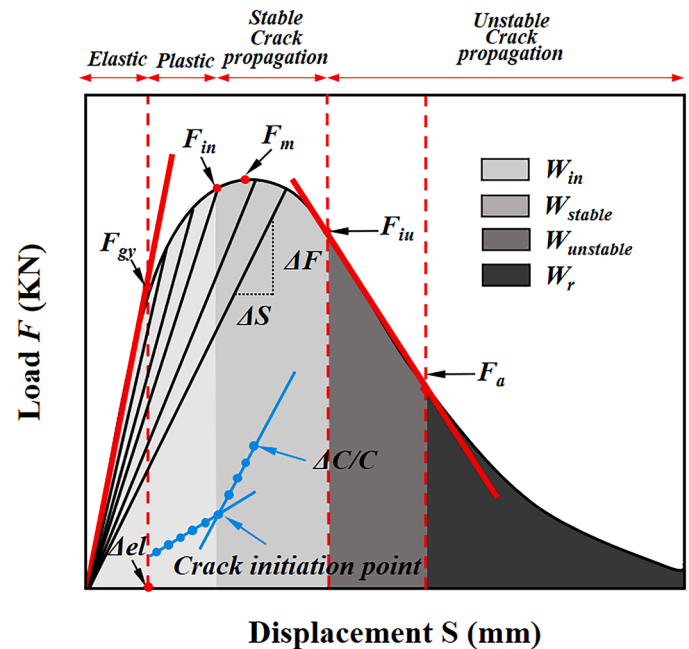

Fig. 2. Schematic diagram showing the absorbed impact energies divided into four different fracture stages for a typical load-displacement curve. In this diagram, W_{in}, W_{stable}, $W_{unstable}$, and W_r denote the energies for crack initiation, stable crack growth, unstable crack growth, and plastic collapse, respectively. Here F_{gy}, F_{in}, F_m, F_{iu}, and F_a correspond to the general yield load, the load at crack initiation, the maximum load, the load at the start of unstable crack growth, and the load at the end of unstable cracking, respectively.

3. Results

3.1. Microstructures

3.1.1. Uniform coarse-grained (CG) and ultrafine-grained (UFG) microstructures

The CG steel (Fig. 3(a1-b2)) plate had uniform equiaxed grains through the thickness with an average size of ~3.76 μm at the surface (~0.3 mm depth) and ~4.03 μm in the core (Fig. 4(a)). The equiaxed grains exhibited a shape factor (average fitted ellipse aspect ratio) of ~2.76 near the surface and ~2.30 in the core (Fig. 4(d)). Further, TEM imaging, shown in Fig. 3(e), revealed that these grains have relatively low dislocation density. The density of high-angle grain boundary (HAGB, misorientation angle θ≥15°) changed slightly from 0.71 μm^{-1} near the surface to 0.64 μm^{-1} in the core (Fig. 4(b-c)), while the density of low-angle grain boundary (LAGB, 2°≤θ<15°) also showed a small variation from 0.32 μm^{-1} to 0.20 μm^{-1}. Pole figures (Fig. 3(c, d)) indicated a weak (112) //ND texture in the CG microstructure.

The UFG steel plate (Fig. 3(f1-g2, j)) had elongated ultrafine-grains through the thickness of roughly uniform sizes ~1.02 and 1.00 μm near the surface (~0.3 mm depth) and in the core, respectively (Fig. 4 (a)). Further, the UFG microstructure consisted of a HAGB density of ~1.42 μm^{-1} near the surface and 1.23 μm^{-1} in the core (Fig. 4(b-c)), whereas the density of the LAGBs respectively was ~0.96 μm^{-1} and 0.81 μm^{-1}. As expected, these grain boundary densities were higher than that of the CG counterpart. Moreover, the shape factor of the grains in the UFG microstructure changed from 5.02 at the surface to 4.19 in the core, which is substantially higher compared to the CG microstructure (Fig. 4 (d)), signifying an elongated bamboo-like morphology in the UFG microstructure. The pole figures in Fig. 3(h-i) showed two distinct textures, (001) ⟨110⟩ and (112) ⟨110⟩, near the surface and in the core of the UFG steel plate.

3.1.2. Microstructure of the heterostructured (HS) steel plate

Fig. 5(a) shows the inverse pole figure (IPF) maps from the surface (depth of ~0 mm) to the core (depth of ~2.5 mm) of the HS steel plate. Examining magnified IPF maps (Fig. 5(A1-D1)), grain boundaries (GB) maps (Fig. 5(A2-D2)) and TEM figures (Fig. 5(b-g)) at different depths
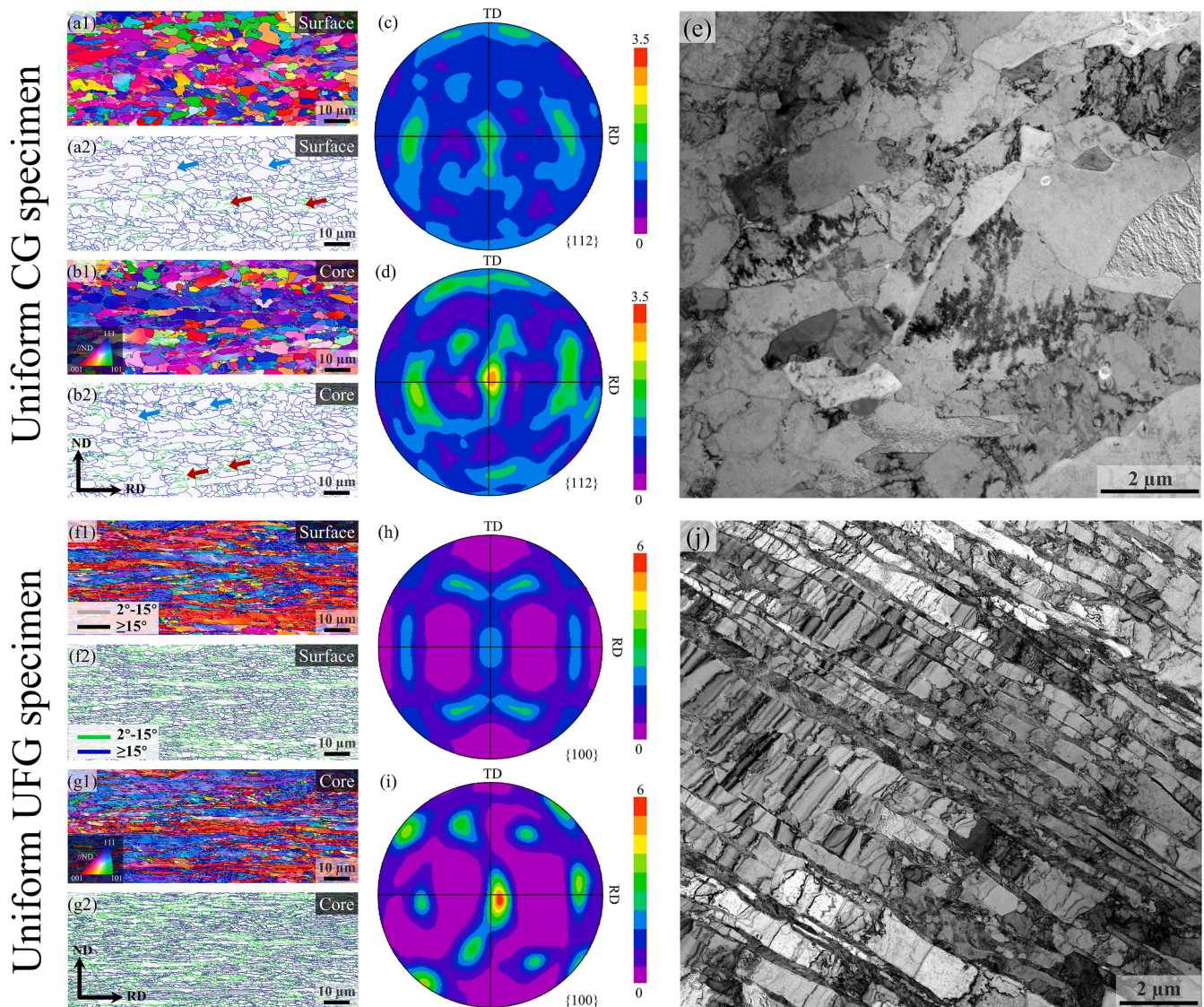

Fig. 3. (a1-a2, b1-b2) Inverse pole figures and grain boundary distribution maps of the uniform CG specimens at the surface (~0.3 mm) and core (~2.5 mm) position of the TD plane (the plane normal to TD). (c, d) Pole figures showing the texture of the corresponding microstructures in (a1, b1). (e) TEM image of the CG microstructure at ~2.5 mm depth from the surface on the TD plane. (f1-f2, g1-g2) Inverse pole figures and grain boundary distribution maps of the UFG microstructure near the surface (~0.3 mm) and core (~2.5 mm) along the TD plane. (h, i) Pole figures of the corresponding in (f1, g1). (j) TEM image of the UFG microstructure at ~2.5 mm depth from the surface on the TD plane.
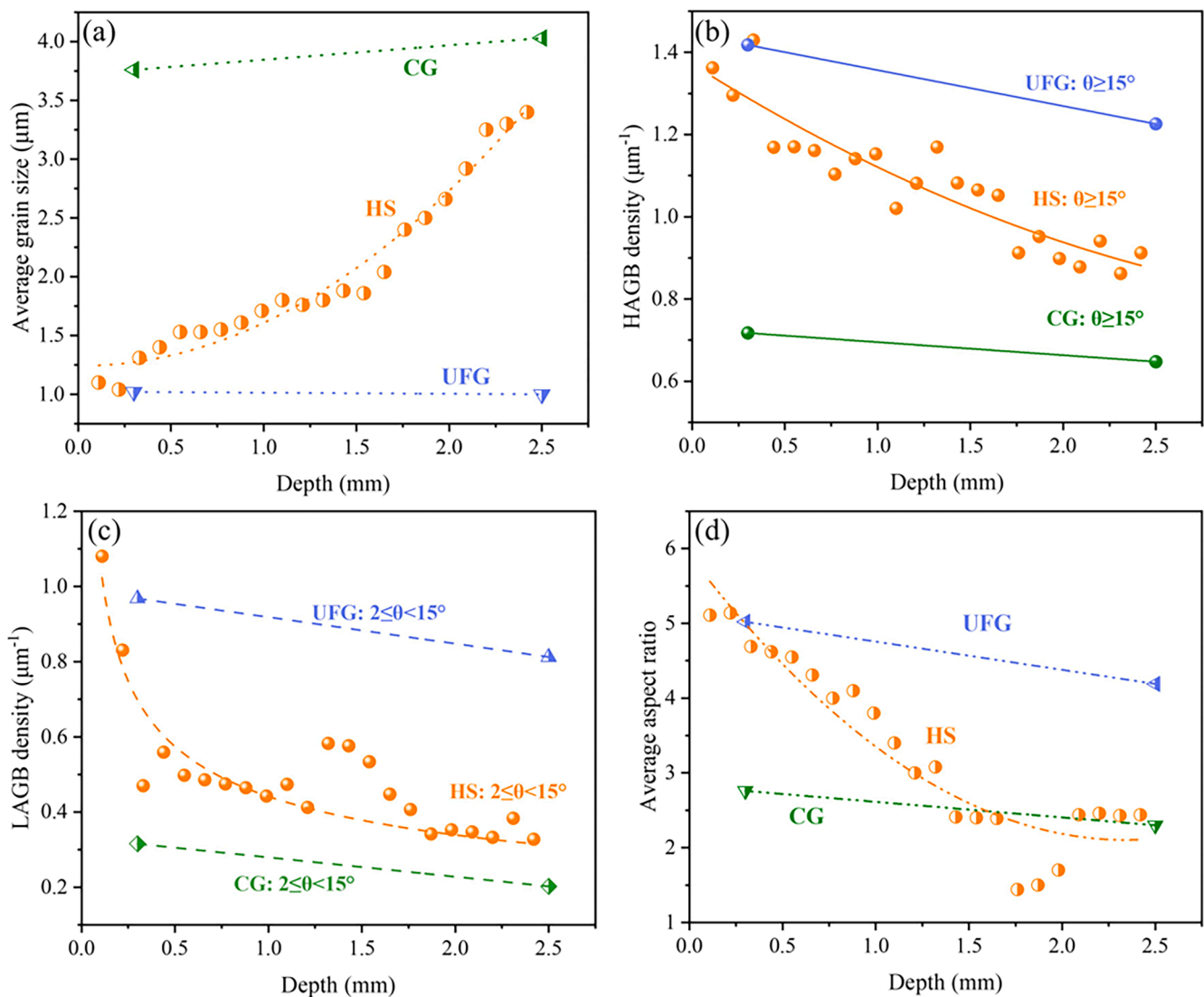
Fig. 4. Variation in (a) average grain size, (b) HAGB density, (c) LAGB density, and (d) average aspect ratio with respect to the thickness of the plate with CG, UFG, and HS microstructures.

documents the variations in grain size, shape, and texture of the HS microstructure. The grain size continuously can be seen to increase from ~1.1 μm near the surface to ~3.4 μm in the core. Concurrently, the densities of HAGBs and LAGBs also showed a gradient in the TD plane. Specifically, the density of the HAGBs (Fig. 4(b)) decreased from ~1.4 μm^{-1} (near surface) to ~0.9 μm^{-1} (in core), while the density of the LAGBs (Fig. 4(c)) decreased from ~1.1 μm^{-1} (near surface) to ~0.3 μm^{-1} (in core). Further, Fig. 4(d) shows the variation in the shape factor of the grains as a function of depth, which decreased from 5.2 to 2.5, indicating a steady shift from elongated ultrafine grains near the surface, to relatively equiaxed coarse grains in the core. In addition, the changes in the color of the IPF map shown in Fig. 5(a) indicate a change in texture across the thickness of the steel plate. The (011) ⟨100⟩ texture near the surface (~0.3 mm depth) changed to (001) ⟨110⟩ texture in the intermediate region (~1.5 mm depth), which further transformed to (112) ⟨110⟩ texture in the core region (~2.5 mm depth) (Fig. S2(a)).

To comprehensively characterize the heterogeneous microstructure of the HS steel plate, EBSD scans on the planes normal to the RD, TD, and ND directions were conducted. The resulting three-dimensional microstructures of the UFG and CG regions of the HS samples are shown in Fig. 5(h-i). Notably, the ultrafine grains near the surface can be divided into two types: spherical ultrafine grains and elongated disk-shaped

grains. Inside the elongated disk-shaped grains, low-angle grain boundaries and sub-grains with an average size of ~1.2 μm were observed (Fig. S2(b)). The ubiquitous sub-grain boundaries are a consequence of dynamic recovery during the hot rolling, which usually occurs in metals with high stacking-fault energy, such as in ferritic steels via dislocation climb and cross-slip mechanisms [37]. The thickness of the grains in the ND (t_{ND}), length in RD (l_{RD}), and TD (l_{TD}) are plotted in Fig. S3. The average values of t_{ND}, l_{TD}, and l_{RD} of the grains are, respectively, 0.87 μm, 1.88 μm, and 3.22 μm near the surface; these values increase by ~200 %, ~23 %, and ~25 %, respectively, in the core region of the plate. This indicates that the refinement of the grains near the surface is primarily restricted to the ND direction because the grains are elongated in the other two directions (RD and TD).

3.2. Mechanical properties

3.2.1. Tensile properties at 293 and 77 K

Fig. 6(a) shows the tensile engineering stress-strain curves of the CG, UFG, and HS microstructures at ambient (293 K) and cryogenic (77 K) temperatures. The corresponding values of yield strength, σ_y, ultimate tensile strength, σ_{uts}, and uniform elongation, ε_u, are summarized in Table 1. At 293 K, the UFG microstructure exhibits a yield strength, σ_y, of
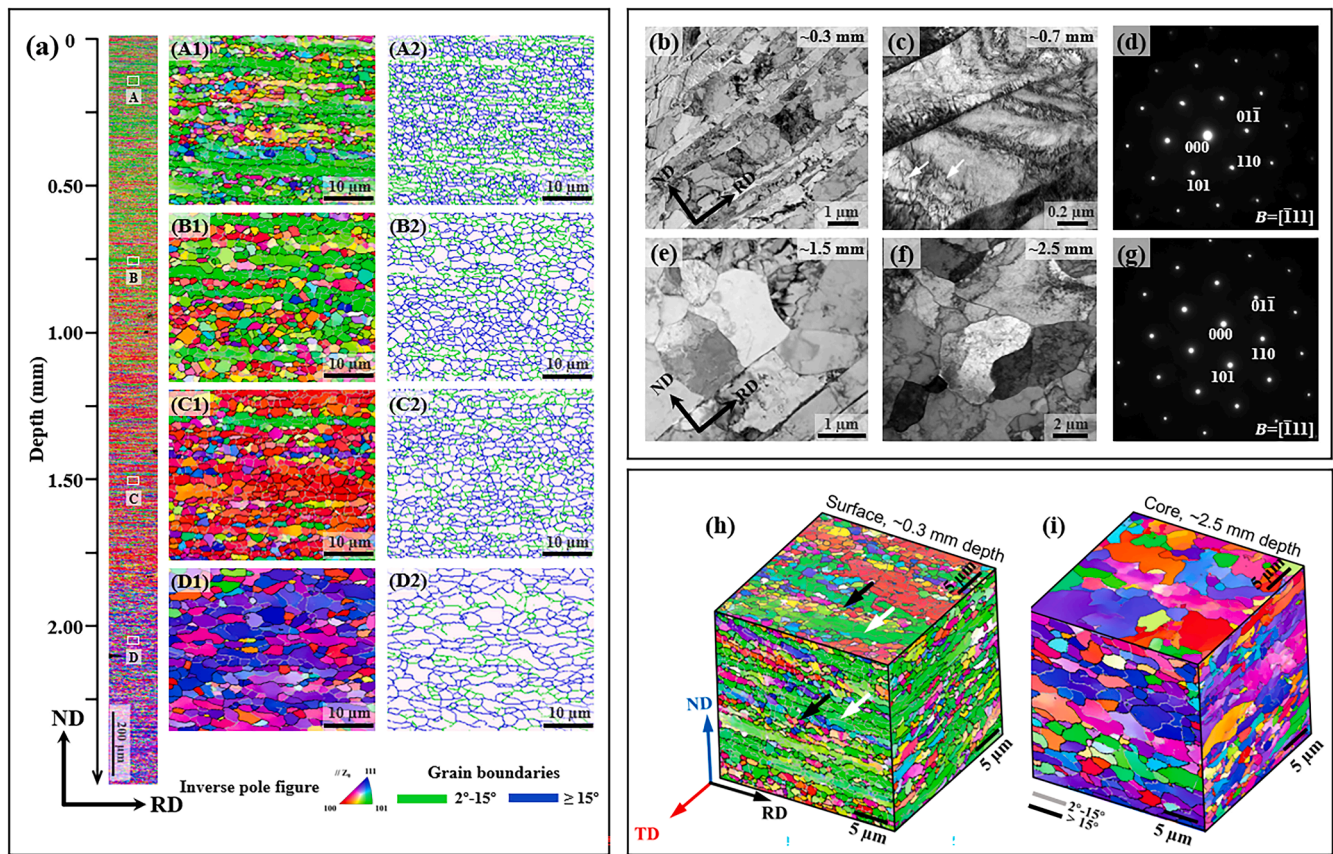
Fig. 5. (a) The EBSD microstructure evolution of the heterostructured HS steel from the surface to the core along the TD plane. (A1–D2) High-magnification inverse pole figures and grain boundary distribution maps at different locations along the thickness of the plate with HS microstructure from locations labeled in (a). TEM images showing the elongated ultrafine grains and dislocations at depths (b) 0.3 mm and (c) 0.7 mm from the surface on the TD plane of the HS microstructure. (d) Selected area diffraction pattern of location shown in (c). TEM images showing relatively equiaxed grains at depths (e) 1.5 mm and (f) 2.5 mm from the surface along the TD plane of the HS microstructure. (g) Selected area diffraction pattern of location shown in (f). Representative pseudo 3D inverse pole figures of (h) UFG region near the surface (~0.3 mm from the surface), and of (i) the core CG region at ~2.5 mm from the surface.
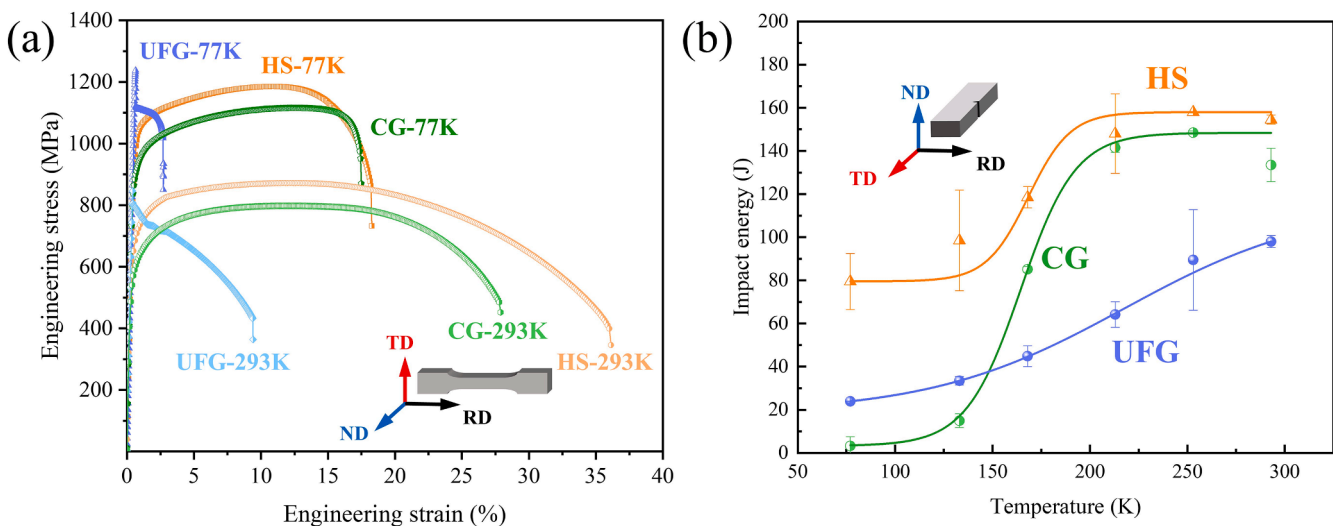
Fig. 6. (a) Engineering stress-strain curves of the CG, UFG, and HS samples obtained at 293 and 77 K. (b) Charpy impact absorbed energy vs. impact-test temperature curves of the CG, UFG, and HS samples.

864 ± 5 MPa and a uniform elongation, ε_u, of 0.4 ± 0.2 %. The yield strength and uniform elongation of the CG microstructure (σ_y 587 ± 15 MPa and ε_u 16.9 ± 2.0 %) is, respectively, 32 % lower and 41 times higher than that of the UFG microstructure. However, the

heterostructured microstructure shows a yield strength, σ_y, of 681 ± 12 MPa, which is 16 % higher than the CG counterpart, without any loss in uniform elongation, i.e., ε_u, 16.8 ± 1.2 %, indicating a high strain hardening ability comparable to the CG sample and significantly higher

Table 1

Tensile properties (σ_y, yield strength; σ_{uts}, ultimate tensile strength; ε_u, uniform elongation) of the CG, UFG, and HS samples.

Sample	293 K			77 K		
	CG	UFG	HS	CG	UFG	HS
σ_y, MPa	587 ± 15	864 ± 5	681 ± 12	914 ± 11	1242 ± 15	1022 ± 7
σ_{uts}, MPa	797 ± 13	807 ± 9	871 ± 10	1115 ± 8	1122 ± 17	1185 ± 14
ε_u,%	16.9 ± 2.0	0.4 ± 0.2	16.8 ± 1.2	14.0 ± 3.0	0.7 ± 0.3	12.3 ± 2.2

than that of the UFG sample (Fig. S4).

At 77 K, the yield strength, σ_y, of the CG microstructure increases by 56 % to 914 ± 11 MPa; however, this is accompanied with a 17 % reduction in uniform elongation to 14.0 ± 3.0 % in comparison to that at 293 K. Moreover, the yield strength, σ_y, of the UFG microstructure is 1242 ± 15 MPa with a negligible uniform elongation, ε_u, of 0.7 ± 0.3 %. In comparison, the HS microstructure at 77 K exhibits a yield strength, σ_y, of 1022 ± 7 MPa, which is 12 % higher than the CG microstructure with a comparable uniform elongation, ε_u, (12.3 ± 2.2 %). These results reveal a strong trade-off between the strength and ductility in the CG and UFG microstructures, whereas the HS microstructure displays an excellent combination of strength and ductility at both 293 and 77 K. This strongly implies that the heterogeneous microstructure promotes a
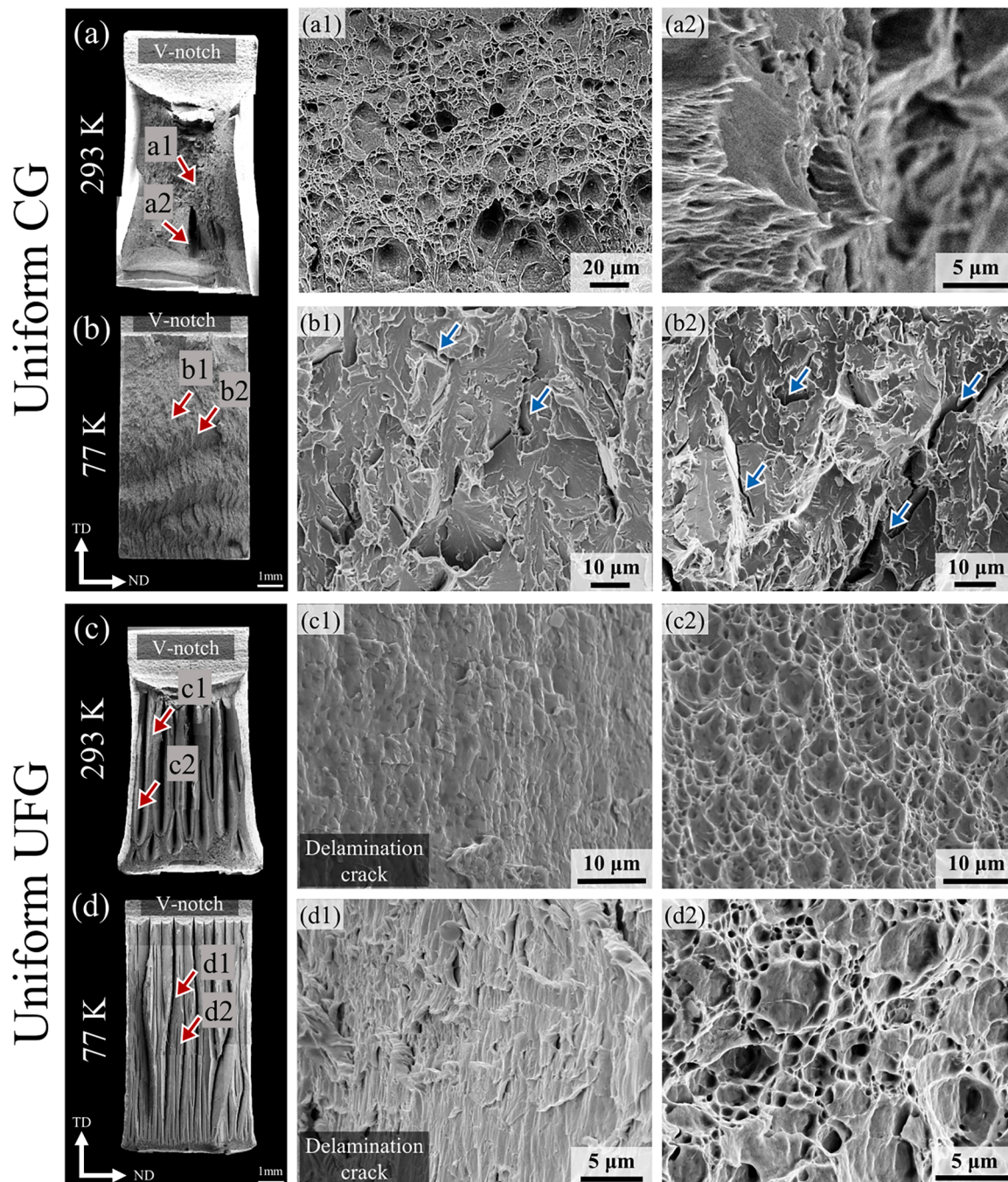
Fig. 7. Fractographs of the impact tested specimens (a, b) CG microstructure and (c, d) UFG microstructure at (a, c) 293 K and (b, d) 77 K, respectively. (a1-a2, b1-b2, c1-c2, d1-d2) are the magnified images of the locations marked in (a-d).

favorable synergy between the strength and ductility under uniaxial quasi-static tensile loading at ambient and cryogenic temperatures.

3.2.2. Charpy impact toughness properties

Fig. 6(b) shows the impact energy-temperature curves for the three microstructures. Notably, at ambient temperature the impact energy of the CG microstructure (148.4 J) is 1.5 times that of the UFG microstructure, although the impact energy drops sharply with decreasing temperature, resulting in 98 % lower value of 3.3 J at 77 K. It should also be noted that the CG microstructure shows 14 % uniform elongation during uniaxial tensile loading at 77 K, whereas it fractures in a brittle manner in V-notched impact tests due to the high-stress triaxiality at the notch tip. The impact energy results of the CG microstructure are consistent with those previously reported for many *bcc* steels, as deformation and failure mechanisms at cryogenic temperatures are sharply dependent on the stress-state [38,39]. The UFG microstructure shows 34 % lower impact energy (98.0 J) at room temperature, whereas it maintains an impact toughness of 23.9 J at 77 K, which is 6.2 times higher than that of the CG counterpart. Similar impact energy-temperature characteristics of UFG and CG microstructures have been reported in other studies [9–11].

In contrast to the above results, the graded HS microstructure shows a superior cryogenic-to-ambient impact toughness compared to its CG and UFG counterparts. In particular, the room temperature impact energy of 158.0 J exceeds that of the CG microstructure by 6 % and that of the UFG microstructure by 61 %. Most importantly, the HS microstructure shows a gradual drop in the impact energy with decreasing temperature, giving rise to an unexpectedly high impact energy of 79.5 J at 77 K, which is 24 times that of the CG structure and 3.3 times that of the UFG structure. These results clearly show that the HS microstructure is resistant to fracture by sudden increases in applied stresses at cryogenic temperatures.

3.2.3. Fracture surface morphology

To investigate the failure mechanisms, the fracture surfaces of the CG, UFG, and HS microstructures were examined after the impact toughness tests. The CG microstructure at 293 K fractures in a ductile manner, with a pronounced stretch zone emanating from the crack tip due to blunting and fracture by microvoid nucleation and coalescence as the crack propagates (Fig. 7(a-a1)). Additionally, a few delamination cracks were observed in the mid-thickness of the CG specimens away from the V-notch (region a2). These delamination cracks form due to elevated triaxial stresses at the test sample's mid-thickness [11]. Since there is limited delamination away from the notch tip, the CG microstructure fails by ductile fracture after extensive plastic deformation at 293 K.

The CG microstructure at 77 K displays brittle fracture with macroscopic flat features (Fig. 7(b)), which is in clear contrast to its ductile nature at 293 K. Regions b1 and b2 in Fig. 7b show transgranular cleavage fracture alongside brittle secondary cracks (marked by the blue arrows). The propagation of cleavage fracture occurs via separation along well-defined crystallographic planes, *e.g.*, {100} planes in ferrite steels, with limited capacity for dissipating energy, leading to catastrophic failures. The CG microstructure subjected to impact tests at both 293 K and 77 K reveals the typical ductile-brittle transition commonly observed in *bcc* steels.

In contrast to the CG microstructure, the UFG microstructure fractures in a ductile mode by microvoid coalescence coupled with delamination at both temperatures (Fig. 7(c-d)). Upon closer examination, the delamination cracks appear to have been formed by grain boundary debonding [9–11]. In the regions between the delamination cracks, numerous ductile dimples sized at ~1–5 μm, are present; indeed, this is a fracture pattern also reported in previous studies on rolled ultrafine grained steels [9–11]. The low-temperature impact toughness of the UFG steel is enhanced by the formation of delamination cracks ahead of the crack tip because the delamination cracks transform the plane-strain

conditions into multiple plane-stress conditions by generating numerous interfaces and promoting limited plasticity [40,41]. Thus, compared to the brittle cleavage fracture, delamination can effectively improve the low-temperature toughness of the *bcc* steels. However, it is important to note that the delamination can weaken energy dissipation capabilities compared to plastic deformation. Additionally, at 77 K compared to 293 K, an increased presence of delamination cracks but reduced plastic deformation was observed. However, in comparison to the distinct ductile to brittle transitions in the CG microstructure, the UFG microstructure displays relatively consistent fracture modes across both temperatures, which is also evident from its gradual loss in impact energy with decreasing temperatures (Fig. 6(b)).

As illustrated in Fig. 8, the graded heterostructured microstructure exhibits a complex fractographic appearance at ambient and cryogenic temperatures, which is quite different from its uniform-grained CG and UFG counterparts. At 293 K, ductile fracture marked by microvoids and shear lips are seen without any delamination (Fig. 8(a1-a2)). In region b, ductile dimples with varying sizes are evident, reflecting the gradient in grain size across the thickness of the HS steel plate (Fig. 8(b)). Indeed, in the core region of the stretch zone, ductile tearing features with dimples of a bimodal distribution are present; the larger dimples are of size of ~20–30 μm, whereas the smaller dimples are ~1–7 μm in size. However, near the surface of the specimens (region d), most dimples are ~1~6 μm in size. In the UFG region near the surface of the HS specimen, a nominal plane-stress condition exists, which promotes significant plastic deformation. The plastic-zone size at the crack tip can be qualitatively estimated from the extent of the shear lip formed [42], where an increased shear lip area indicates an expanded plastic-zone size, and enhanced toughness [42,43]. Indeed, the variability in strain and stress-state inherent to the gradient microstructure not only promotes extensive plastic deformation in the UFG region near the surface but also alleviates the stress concentration in the CG region near the core.

At 77 K, the UFG region of the heterostructured microstructure shows long and straight extensive delamination cracks during fracture (Fig. 8(e1-e2)), where the alternating sequences of delamination and dimple fracture closely resemble the fracture mode of UFG microstructure tested at 77 K (Fig. 8(g-h)). Similarly, the newly generated interfaces and alleviated triaxial stress are effective at low temperatures in increasing the toughness compared to the brittle fracture. In contrast, the CG region of the HS microstructure has sporadic short delamination cracks (Fig. 8(e1-e2, i)). Unlike the flat cleavage fracture observed in the CG specimen at 77 K, the core CG region of the HS microstructure exhibits ductile dimple fracture by plastic deformation with an obvious shear strain feature (Fig. 8(e2, j-k)). Here the plastic deformation in the core region with coarse grains serves as the primary driver behind the three-fold increase in impact toughness compared to the UFG microstructure. While delamination cracks in the UFG region near the surface are expected, the extensive plastic deformation in the coarse-grained core region is surprising and points to a change in the deformation mechanisms owing to the heterogeneous microstructure.

3.3. Impact resistance

The impact energies of the CG, UFG, and HS microstructures at 293 K and 77 K show significant variation. Therefore, instrumented Charpy impact tests for each condition were performed to understand the role of the resistance to crack initiation and growth at the different stages of fracture. The energies for these stages are divided into crack-initiation energy (W_{in}), stable crack-growth energy (W_{stable}), and unstable crack-growth energy ($W_{unstable}$). These energies were measured using the compliance change rate (CCR) method; details are described in Fig. 2 and the Supplementary Materials. To further understand the fracture behavior, dynamic *J*-R curves, derived from the nonlinear-elastic fracture mechanics model described in the Supplementary Materials, were determined from the load-displacement data. Figs. 9(a, b) show that both the UFG and HS microstructures require a relatively higher load
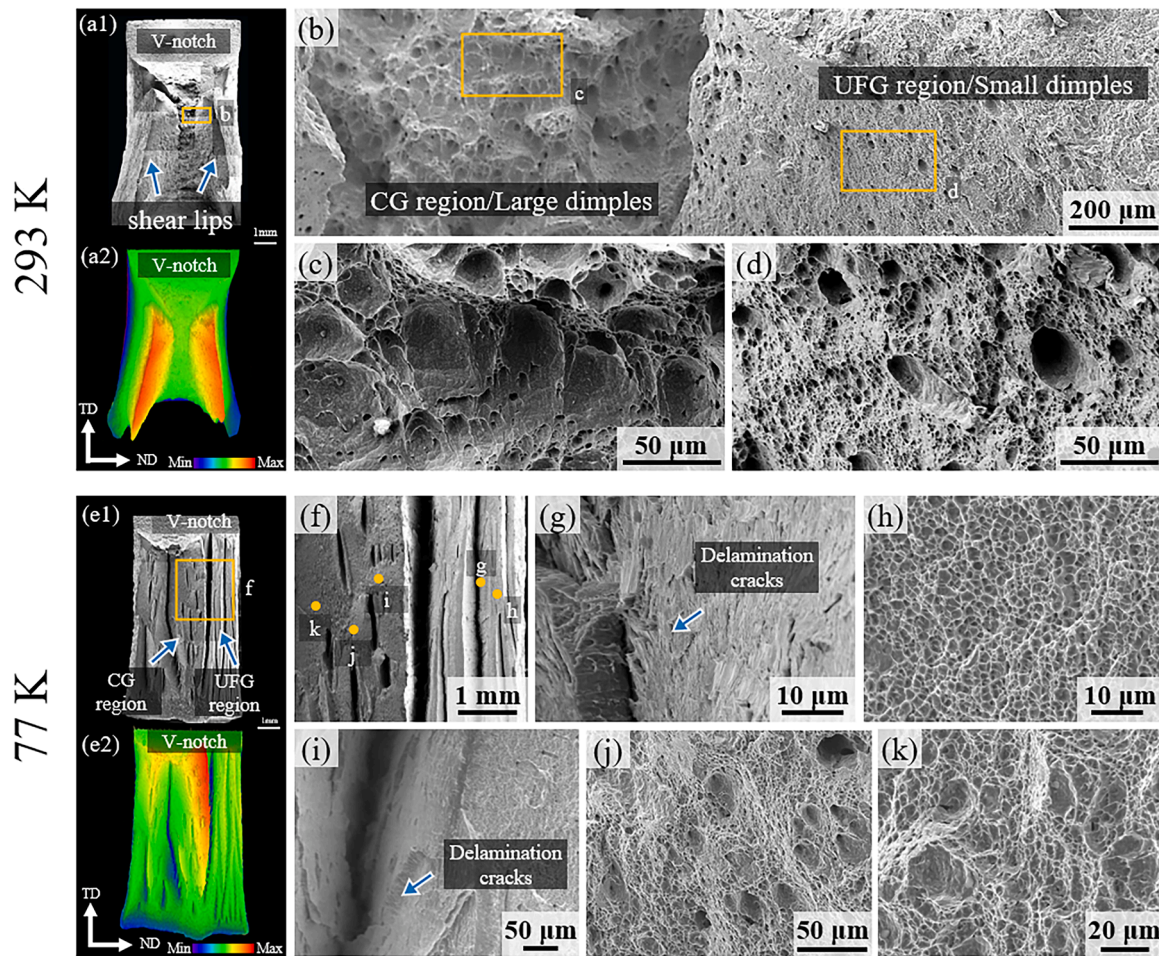
Fig. 8. Fractographs of the impact-tested HS microstructures at 293 K and 77 K, respectively. (a1-a2) The fracture surface of the HS microstructure at 293 K shows full ductile fracture features with large shear lips. (b) The magnified image of locations marked in (a) shows a gradient in dimple size from the surface to the core of the HS specimen. (c-d) Magnified images of locations marked in (b) showing the dimples in the core CG region and the UFG region near the surface. (e1-e2) Fracture surface of the HS specimen at 77 K. (f) The magnified image of the location marked in (e1) showing the long and straight delamination cracks in the UFG region near the surface and sporadic short delamination cracks in the core CG region. (g-h) Magnified images of locations marked in (f) showing the long and straight delamination crack and dimples in UFG region near the surface. (i-k) Magnified images of locations marked in (f) showing the sporadic short delamination cracks and dimples in the core CG region.

(and hence energy) to initiate cracks than the CG microstructure. However, as shown in Fig. 9(c), for all the microstructures, the difference in the crack-initiation and unstable crack-growth energies is marginal at 293 K, indicating their influence on the impact toughness is secondary. In contrast, the stable crack-growth energy varies significantly with microstructure and temperature conditions. For example, the stable crack-growth energy W_{stable} for the UFG microstructure (~32.1 ± 2.2 J) is considerably lower than that for its CG structure (~83.9 ± 5.3 J), underlying its inferior impact resistance. Of note though is that the heterogeneous microstructure demonstrates the highest W_{stable} (~88.0 ± 5.2 J), outperforming that of the UFG and the CG microstructures by 174 % and 5 %, respectively, at 293 K.

The J-integral crack-resistance curve (J-R curve), based on nonlinear-elastic fracture mechanics, is frequently used to evaluate the energy dissipation and the fracture resistance of materials as a function of crack extension [21,22]. To further evaluate the fracture resistances of the CG, UFG, and HS samples under the impact loading, we estimated the J-R curves from the load-displacement data recorded during instrumented impact tests. As shown in Fig. 9(e), the crack initiation toughness (Δa ~ 0.2 mm secant line intersection with J-R curve) of CG, UFG, and HS microstructures are 2099, 1585, and 2513 kJ·m^{-2}, respectively. Although the initiation toughness values obtained by dynamic J-R tests are conditional and depend on the thickness of the

specimens, the differences in the values can be used for comparative analysis. The high crack-initiation toughness in all cases points to typical ductile behavior of these microstructures at room temperature. Furthermore, the relatively muted increase in J to ~1750 kJ·m^{-2} after 1.5 mm of crack extension Δa (sometimes termed the steady-state J_{ss}) in the UFG microstructure points to its low resistance to crack propagation, i.e., its poor damage tolerance. In contrast, the dynamic J-R curves of both the CG and HS microstructures show a steep (rising) increase. At Δa ~ 1.5 mm, the value of the crack-driving force J_{ss} is ~3250 kJ·m^{-2} and ~3500 kJ·m^{-2} for the CG and HS microstructures, respectively.

At 77 K, the CG microstructure exhibits brittle behavior as indicated by its low impact energies, W_{in}, W_{stable}, and $W_{unstable}$, ~1.1 ± 0.2 J, ~1.3 ± 0.2 J, and ~0.6 ± 0.1 J, respectively. In contrast, the UFG microstructure shows a markedly higher, W_{in} ~6.4 ± 1.0 J, W_{stable} ~6.4 ± 1.2 J, and $W_{unstable}$ ~3.8 ± 0.7 J, respectively. The heterogeneous HS microstructure stands out with W_{in} ~12.9 ± 2.1 J, which is ~10.7 and ~1.0 times higher than that of CG and UFG microstructures, respectively. Furthermore, the HS microstructure also demonstrated a W_{stable} ~26.5 J, which is 19.4 times and 3.1 times higher than the CG and UFG microstructures, respectively. At 77 K, the dynamic J-R curves (Fig. 9(f)) show the initiation toughness for the CG, UFG, and HS microstructures as ~51, 360, and 680 kJ·m^{-2}, respectively. These values are markedly different, reflecting their resistance to crack propagation at cryogenic
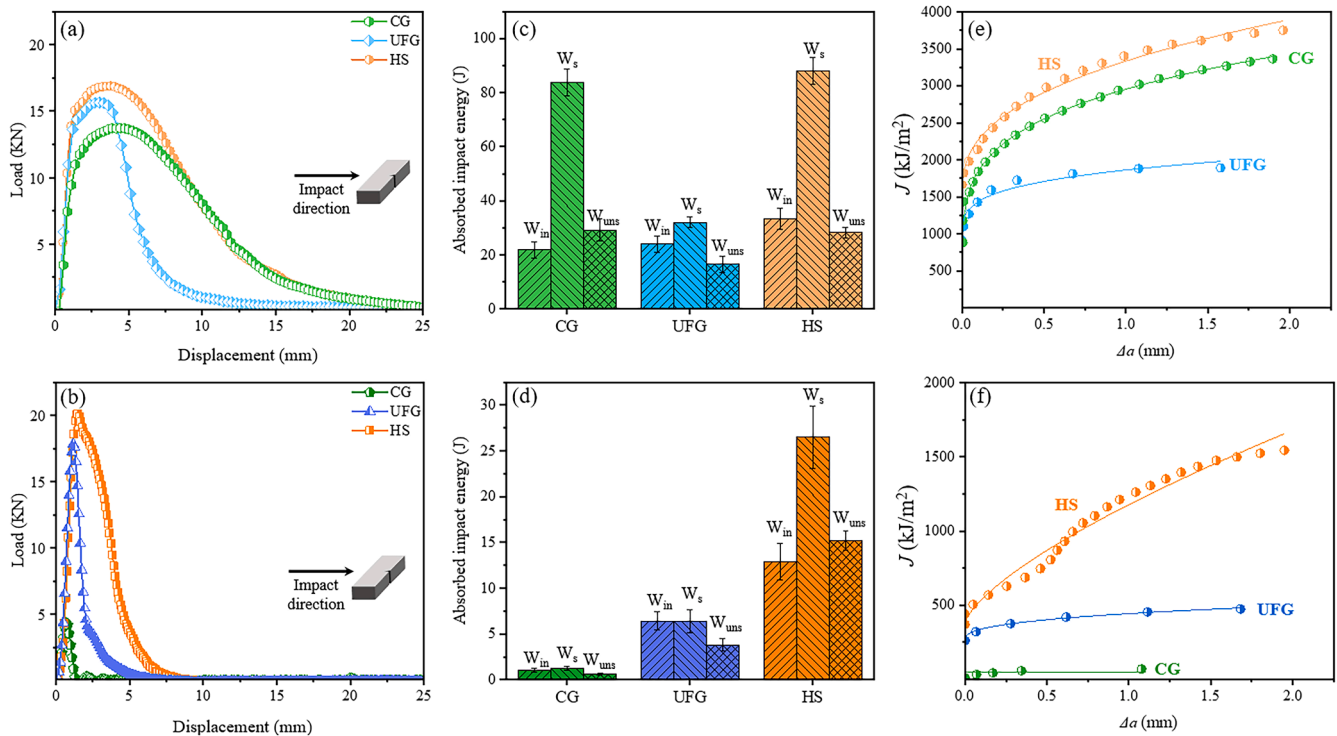
Fig. 9. Load-displacement curves of the CG, UFG, and HS V-notched samples obtained from instrumented Charpy impact tests at (a) 293 K and (b) 77 K. Absorbed impact energies at crack initiation, stable growth, and unstable growth of the various samples at (c) 293 K and (d) 77 K. Dynamic J-R curves at (e) 293 K and (f) 77 K, showing the variation in the value of J to sustain crack extension Δa, for the CG, UFG, and HS microstructures under impact loading.

temperatures. Furthermore, with crack extension, the resistance to crack growth increases steeply in the HS microstructure unlike the CG and UFG counterparts. After ~1.5 mm of crack extension, the J_{ss} values for the CG and UFG microstructures remain constant; however, the J_{ss} of the HS microstructure increases to 1500 kJ·m^{-2} from 680 kJ·m^{-2} at Δa ~0.2 mm.

The energy spent in different stages of fracture indicates that the surprisingly high impact toughness displayed by the HS microstructure could be primarily related to the energy spent in a stable crack growth, W_{stable}, at room temperature. Simultaneously, the remarkable cryogenic impact resistance of the HS microstructure seems to have been substantially influenced by both the energy utilized in crack initiation and growth.

4. Discussion

Generally, there are two major classes of toughening: intrinsic and extrinsic toughening mechanisms [44–46]. Intrinsic toughening is prominent ahead of the crack tip and can be enhanced by increasing the plasticity and work hardening capacity of materials, which can promote their resistance to crack initiation and growth. Extrinsic toughening, conversely, occurs at behind the crack tip, and is associated with crack-tip shielding by mechanisms such as crack bridging, deflection, and delamination, all of which serve to lead to the reduction of local stresses and strains at the crack tip [44–46]. In this section, the possible underlying toughening mechanisms responsible for the excellent cryogenic impact toughness of the heterogeneous structure are discussed.

4.1. Intrinsic toughening mechanisms of HS structure under the dynamic impact loading at 77 K

For heterogeneous structures, it has been reported that their deformation can be highly inhomogeneous [19,25,47–51]. The inhomogeneous deformation is accommodated by the pile-up of long-range

geometrically necessary dislocations (GNDs), which act to induce an extra work hardening capability, termed hetero-deformation induced (HDI) hardening, hence improving intrinsic microstructural resistance to fracture [47–51]. However, such inhomogeneous deformation under high strain-rate loading at cryogenic temperature has rarely been reported before. To verify the heterogeneous deformation behavior of our present HS steel during such impact loading, interrupted impact tests with fixed energy input of ~10 J and ~32 J were performed at 77 K (Fig. S5); the resulting microstructure evolution around the notch is presented in Fig. 10.

At an impact energy of 10 J at 77 K, slight deformation without any delamination cracks was observed around the V-notch. As shown in Fig. 10(a-b1), a significant increase in the density of grain boundaries, particularly in the LAGBs within the grains, was observed, although slight changes in the grain morphology, such as grain shape and size, were detected in the core CG region (mid-thickness) at ~0.5 mm distance from the V-notch. This suggests the occurrence of dislocation multiplication and interactions leading to the formation of cell substructures (Fig. 10(b2), Fig. S6(a)) [37,52–54]. Statistical analysis data shown in Fig. 11 revealed that the densities of the LAGBs (3.1 μm^{-1}) and HAGBs (2.2 μm^{-1}) in the CG region were ~9.3 and 0.6 times higher than those of the undeformed microstructure (0 J), respectively. Compared with the CG region, the densities of the LAGBs (3.1 μm^{-1}) and HAGBs (2.0 μm^{-1}) in the UFG region at 10 J were only 1.4 and 0.3 times higher than those of the undeformed microstructure (Fig. 10(c-d2), Fig. 11, Fig. S6(b)). The higher increment in grain boundary density in the CG region compared to the UFG region after the 10 J-impact at 77 K indicates a more pronounced microstructure refinement and plastic deformation within the coarse grains, confirming inhomogeneous distribution of strain even at the initial stage of impact loading.

With increasing energy to 32 J, the inhomogeneous strain distribution was more obvious between CG and UFG regions (Fig. 10(e-h2)). As shown in Fig. 10(f1-f2), a significant alteration in the grain morphology was observed in the CG region; the grains were elongated with their
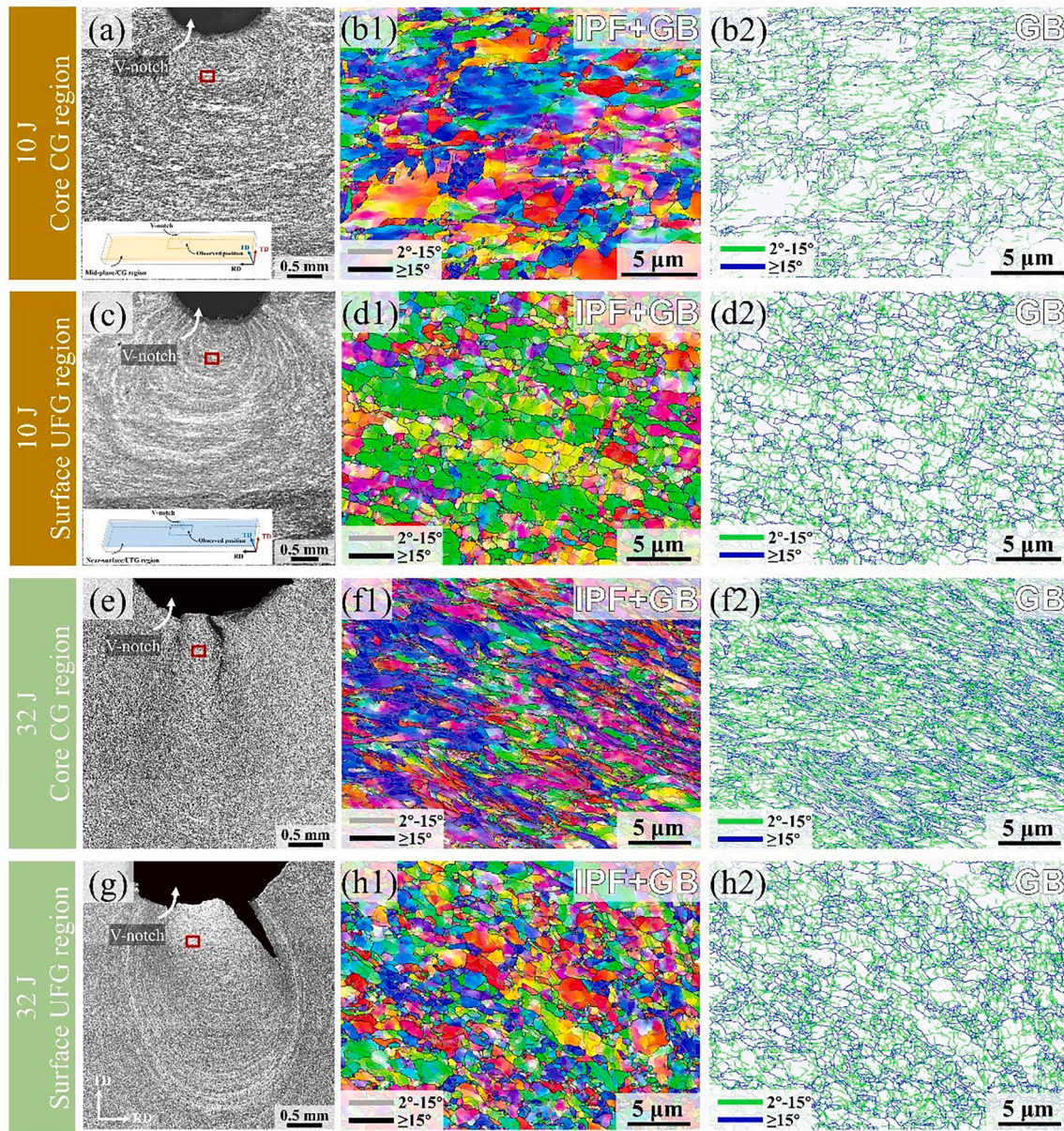
Fig. 10. Deformed microstructure of the HS microstructure after V-notch impact testing with different input energy. The deformed microstructure of the (a) core region and (c) surface region after a 10 J-impact at 77 K. (b1-b2) IPF and GB maps highlighting the grain boundaries and deformation features at the position indicated by the red box in (a). (d1-d2) IPF and GB maps showing the grain boundaries and deformation features for the position labeled by the red box in (c). Deformed microstructure of the (e) core region and (g) surface region after a 32 J-impact at 77 K. (f1-f2) The IPF and GB maps highlighting the grain boundaries and deformation features at the position indicated by the red box in (e). (h1-h2) IPF and GB maps showing the grain boundaries and deformation features of the position labeled by the red box in (g).

aspect ratio increased from 2.3 to 3.5, while the grain morphology in the UFG region remained essentially the same. The densities of LAGBs and HAGBs in the CG region increased to 5.5 μm^{-1} and 3.9 μm^{-1}, respectively, i.e., 17.3 and 1.8 times higher than in the undeformed microstructure, while the increments in LAGB (3.9 μm^{-1}) and HAGB (2.5 μm^{-1}) densities in the UFG region remained only 2 and 0.7 times higher, which is significantly lower than those in the core CG region (Fig. 11). Overall, the average LAGB and HAGB density increase rates in the CG region were 0.16 μm^{-1}/J and 0.07 μm^{-1}/J, respectively, which are approximately doubled compared with the UFG region (0.08 μm^{-1}/J of LAGB and 0.03 μm^{-1}/J of HAGB). These results confirm that the strain in the CG region is much higher than that of UFG regions at an impact energy of 32 J.

It is clear from these results that the core CG region carries more plastic strain than the surface UFG region in the heterogeneous structures during the impact test at 77 K [43,51]. Furthermore, the inhomogeneous gradient distribution of strain becomes more apparent with increasing input energy. To maintain the continuity of the interfaces, GNDs will accumulate and produce long-range internal HDI stress [19, 25,49–50]. Therefore, additional work hardening capacity can be inferred from the HDI hardening in the HS structure, which eventually contributes to an intrinsic higher resistance to fracture.

4.2. Extrinsic toughening mechanisms of HS structure under the dynamic impact loading at 77 K

Delamination is an extrinsic toughening mechanism that is especially effective in improving the low-temperature toughness of certain *bcc*
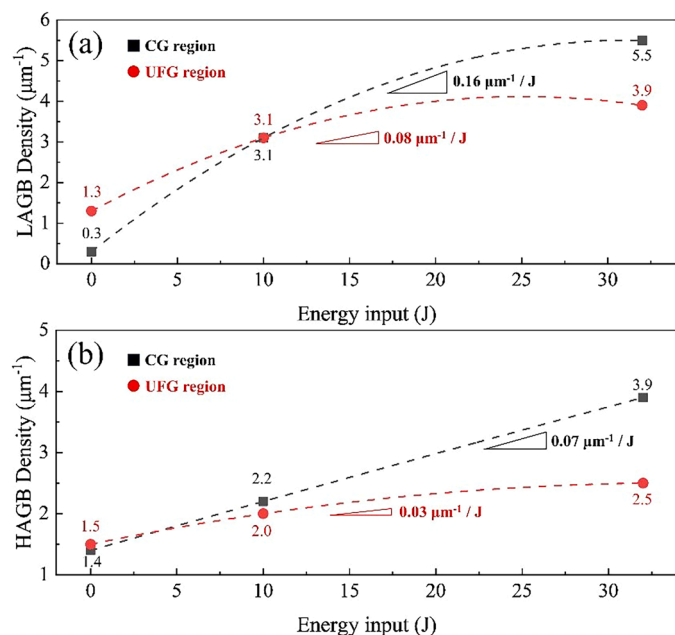
Fig. 11. A summary plot showing the variation of (a) LAGB density and (b) HAGB density as a function of energy input during impact loading at 77 K.

steels and high-strength steel. For example, Song et al. found that the low-temperature toughness of delaminated low carbon ultrafine-grained steel was three times higher than that of coarse-grained steel, similar to the fracture behavior of uniform UFG and CG steels observed in this study [10]. Liu *et al.* achieved a fracture toughness (K_{JIc}) of 101.5 MPa•m$^{1/2}$ by activating delamination in a medium Mn steel while maintaining a strength level of 2 GPa [41]. The mechanism of delamination toughening is attributed to two primary factors. Firstly, the delamination can consume more energy by increasing the crack path tortuosity to produce new interfaces. Secondly, it promotes plastic deformation by decreasing the stress triaxiality at the delaminated ligament tip (Fig. S7), i.e., it promotes a series of local plane-stress conditions to replace a single plane-strain condition [9,10,40,41]. Fracture surface analysis results from Fig. 8 suggest that delamination toughening was also activated in HS steel at 77 K, but its mode appears to be different from that of uniform UFG steel. Thus, we examined the cross-section (TD plane) near the notch tip of impacted specimens to gain a deeper understanding of the extrinsic delamination toughening with the three CG, UFG, and HS microstructures.

4.2.1. Fracture and delamination mode in the homogeneous structures

Of the three microstructures, the CG microstructure has the lowest impact energy at 77 K with a side view of the fracture surface showing no delamination cracks (Fig. S8(a)). Furthermore, IPF and kernel average misorientation (KAM) maps (Fig. S8(c1-e2)) obtained from locations as marked in Fig. S8(a) show no grain refinement or detectable plastic deformation in the grains. These results indicate that the CG microstructure failed by cleavage during dynamic impact loading at 77 K without little to no extrinsic toughening.

In contrast, the side view of the fracture surface of the UFG specimen at 77 K (Fig. S9(a)) shows multiple delamination cracks with different depths. Based on the depth of the delamination cracks, they are classified into two groups: (i) shallow delamination cracks of depth ~0.2 to 1 mm uniformly distributed along the thickness (blue arrows in Fig. S9 (a)), and (ii) a deep delamination crack of depth of ~4.7 mm located at the mid-thickness (red arrow in Fig. S9(a)). In addition, the delaminated ligaments ruptured by shearing at angles of ~42° to 70° (Fig. S9(a)) indicate fracture in regions of low stress-triaxiality [38]. As a consequence, the tip of the delaminated ligament shows obvious plastic

deformation with the grain thickness reduced from ~744 nm in the undeformed region (Fig. S9(d1-d2)) to ~384 nm in the deformed microstructure (Fig. S9(c1-c2)). The IPFs in Fig. S9(e1-e2) confirm that the delamination cracks preferably form in the high-angle grain boundaries separating columns of elongated grains, which is consistent with previous studies [9,10] (Fig. S9(e2)). This fracture mode of the UFG microstructure resulted in ~6 times higher impact energy compared to the CG microstructure at 77 K. In addition, the number of delamination cracks in the UFG microstructures was reduced at 293 K, although their depth remained similar to one deep delamination crack in the mid-thickness (Fig. S10). While the long cracks in the center of the plates are possibly forming due to the higher stress-triaxiality in the center, the disparity in the extent of delamination between 293 K and 77 K can be attributed to the distinct plastic deformation capabilities of the microstructures at these temperatures.

### 4.2.2. Delamination behavior in the HS structure

The HS microstructure shows distinct delamination behavior compared to the CG and UFG microstructures (Fig. 12(a)). On the one hand, the specimen with the HS microstructure displays two deep delamination cracks of depth ~2.6 mm and ~4.2 mm distributed on both sides, rather than solely at the mid-thickness. The shallow delamination cracks (marked by the blue arrows in Fig. 12(a)) in the UFG region of the HS microstructure are similar to those observed in specimens with uniform UFG microstructures. EBSD maps from the tip of the delaminated ligament in the UFG region (Fig. 12(c1-c2)) show plastic deformation within regions of refined grain thickness (of ~410 nm); detailed examination indicates that the delamination cracks are also preferably generated along the grain boundaries (Fig. 12(d1-d2)). High-angle annular dark-field (HADDF) and EDS maps (Fig. 12(e1-e5)) show evidence of the segregation of carbon (C), manganese (Mn), and chromium (Cr) to these boundaries. Additionally, the long delamination crack was found to be located in the transition zone between different textures, with (001) ⟨110⟩ and (112) ⟨110⟩ textures on either side (Fig. 12(d3-d4)). All these assisted the formation of deep delamination cracks in the heterogeneous microstructure. In contrast, the CG region shows severe plastic deformation with the grain diameter d_g reduced from ~2–3 μm in the undeformed region (Fig. 12(g1-g2)) to ~870 nm in the deformed microstructure (Fig. 12(f1-f2)). The severe plastic deformation in the CG region of the HS specimen was derived from the decreased stress-triaxiality (shear angles of ~32°) by the delamination. All of these factors contributed to the three-fold increase in the impact toughness of the heterogeneous material at 77 K compared to uniform UFG specimens. In conclusion, the extrinsic delamination toughening featuring two deep delamination cracks in the HS specimen not only generated new interfaces to consume energy but also promoted plastic deformation by reducing triaxial stresses in the core CG region to further enhance the cryogenic toughness.

4.3. Plainification in steel

The traditional method to enhance the cryogenic toughness of steels has typically involved expensive alloy additions, specifically Ni and Mn. However, in practice, these additions not only inflate the cost of steel production but also pose substantial complications in terms of recycling due to their high content. Our current study here provides an alternative to this through microstructural modification. The present study demonstrates that the heterostructured steel, without any significant alloying additions (0.05C-0.55 Ni-1.95 Mn wt.%), exhibits mechanical properties that fulfill the same requirements as the more expensive 9Ni steel (Table S1) [55]. Specifically, Fig. 13 shows the Charpy impact toughness (J/cm^2) of the HS microstructure at cryogenic temperatures in comparison to other high-Ni/Mn steels [56–67]. Usually, the impact toughness of steels linearly increases with increasing Ni/Mn content. However, the HS microstructure exhibits a cryogenic impact toughness, which is comparable to that of high Ni/Mn steels. These results
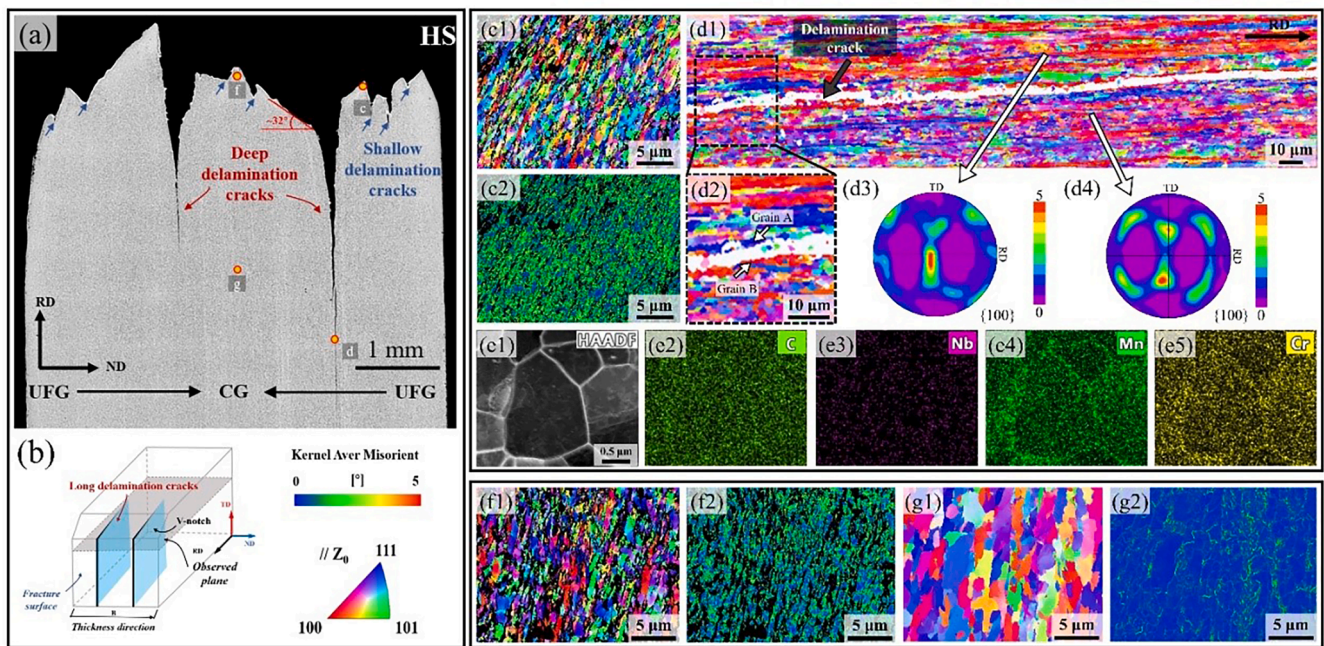
Fig. 12. (a) Through-thickness crack-path viewed from the TD plane of the HS samples fractured at 77 K during impact loading. (b) Schematic of the fractured specimens showing the section selected for the microstructure characterizations. (c1–c2) IPF and KAM maps of the deformation features in the UFG region of the location marked in (a). (d1–d4) IPF and pole figures showing the microstructure and texture near the deep delamination crack. (e1-e5) HAADF-STEM image and element maps show the segregation of C, Mn, and Cr near the delamination crack tip. (f1-f2) IPF and KAM maps show the deformation features near the fracture surface in the CG region of the location marked in (a). (g1-g2) IPF and KAM maps showing the microstructure of CG region far away from the fracture surface.
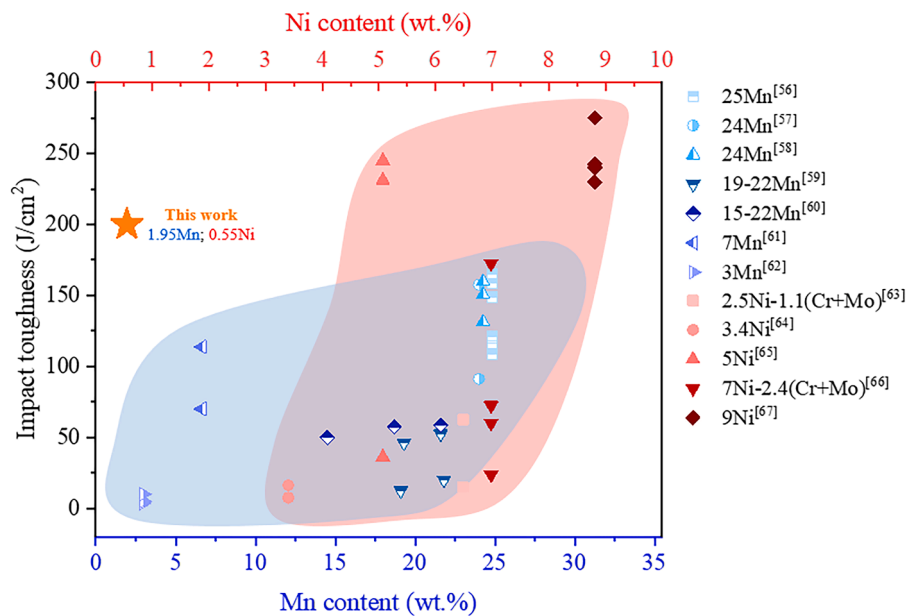
Fig. 13. Plot showing a comparison between the impact toughness of steels at 77 K and the Ni/Mn contents, illustrating the trade-off in cryogenic toughness-alloy content for both commercially available Ni/Mn-containing steels from the literature [56–67] and the heterogeneous microstructure investigated here.

demonstrate a viable example of plainification with improved mechanical properties.

5. Summary and conclusions

In summary, a bulk 5-mm thick low carbon micro-alloyed alloy steel plate was synthesized by a unique rolling strategy coupled with an ultrafast cooling process to produce microstructure with gradients in grain size, morphology, and texture. The strength, ductility, and dynamic fracture resistance of this heterogeneous microstructure (HS), in comparison with coarse-grained (CG) and ultrafine-grained (UFG) structures, was examined at temperatures ranging from ambient to liquid nitrogen temperatures. The HS microstructure was found to display an optimal combination of strength, ductility, and impact toughness at ambient temperature (293 K). Moreover, this microstructure exhibited outstanding cryogenic impact toughness ($\sim$200 J/cm^2) at 77 K, which is $\sim$24 times higher than that of the CG steel and $\sim$3 times higher than the UFG microstructure. During impact loading at cryogenic temperatures,

the deformation of the HS steel plate generated progressive cell substructure formation from the core to the surface, which resulted in a refined microstructure accompanied by extra hetero deformation-induced (HDI) hardening to improve intrinsic toughening. Moreover, the subsequent delamination process along the boundaries of the coarse grains in the core region of the HS samples and in the ultrafine-grained regions near their surfaces served to reduce the stress-triaxiality, thereby facilitating plastic deformation in the CG core region of the HS microstructure. Such delamination also promoted ductile fracture in the latter regions, leading to increased work hardening and improved extrinsic toughening by shielding and blunting of the cracks. The outstanding impact toughness exhibited by the HS microstructure shows the potential of low carbon micro-alloyed (LCMA) steels to be adopted for extremely low-temperature applications. Moreover, the microstructural design strategy aligns with the ongoing efforts toward the development of sustainable materials through plainification.

CRediT authorship contribution statement

Xiaoning Xu: Data curation, Visualization, Writing – original draft. **Punit Kumar:** Formal analysis, Writing – original draft. **Ruqing Cao:** Investigation, Writing – review & editing. **Qibin Ye:** Conceptualization, Investigation. **Yuexin Chu:** Investigation, Writing – review & editing. **Yong Tian:** Conceptualization, Writing – review & editing. **Yi Li:** Conceptualization, Writing – review & editing. **Robert O. Ritchie:** Conceptualization, Writing – review & editing.

Declaration of Competing Interest

The authors declare that they have no known competing financial interests or personal relationships that could have appeared to influence the work reported in this paper.

Acknowledgments

Supplementary materials

Supplementary material associated with this article can be found, in the online version, at doi:10.1016/j.actamat.2024.120019.

References

[1] J.W. Morris Jr, Materials science - Stronger, tougher steels, Science 320 (2008) 1022–1023.
[2] Y. Kimura, T. Inoue, F. Yin, K. Tsuzaki, Inverse temperature dependence of toughness in an ultrafine grain-structure steel, Science 320 (2008) 1057–1060.
[3] H. Zhang, M. Sun, Y. Liu, D. Ma, B. Xu, M. Huang, D. Li, Y. Li, Ultrafine-grained dual-phase maraging steel with high strength and excellent cryogenic toughness, Acta Mater 211 (2021) 1–14.
[4] H. Ding, Y. Wu, Q. Lu, P. Xu, J. Zheng, L. Wei, Tensile properties and impact toughness of S30408 stainless steel and its welded joints at cryogenic temperatures, Cryogenics (Guildf) 92 (2018) 50–59.
[5] X.N. Cheng, Q.X. Dai, A.D. Wang, L. Cheng, Effect of alloying elements and temperature on impact toughness of cryogenic austenitic steels, Mater. Sci. Eng. A 311 (2001) 211–216.
[6] H. Kim, Y. Ha, K.H. Kwon, M. Kang, N.J. Kim, S. Lee, Interpretation of cryogenic-temperature Charpy impact toughness by microstructural evolution of dynamically

[7] Y. Lu, Y.H. Zhang, E. Ma, W.Z. Han, Relative mobility of screw versus edge dislocations controls the ductile-to-brittle transition in metals, P. Natl. Acad. Sci. U. S.A. 118 (2021) 1–6.
[8] X.Y. Li, K. Lu, Improving sustainability with simpler alloys, Science 364 (2019) 733–734.
[9] R. Song, D. Ponge, D. Raabe, J.G. Speer, D.K. Madock, Overview of processing, microstructure and mechanical properties of ultrafine grained bcc steels, Mater. Sci. Eng. A 441 (2006) 1–17.
[10] R. Song, D. Ponge, D. Raabe, Mechanical properties of an ultrafine grained C-Mn steel processed by warm deformation and annealing, Acta Mater 53 (2005) 4881–4892.
[11] X.J. Shen, S. Tang, Y.J. Wu, X.L. Yang, J. Chen, Z.Y. Liu, R.D.K. Misra, G.D. Wang, Evolution of microstructure and crystallographic texture of microalloyed steel during warm rolling in dual phase region and their influence on mechanical properties, Mater. Sci. Eng. A 685 (2017) 194–204.
[12] N. Tsuji, R. Gholizadeh, R. Ueji, N. Kamikawa, L. Zhao, Y. Tian, Y. Bai, A. Shibata, Formation mechanism of ultrafine grained microstructures: various possibilities for fabricating bulk nanostructured metals and alloys, Mater. Trans. 60 (2019) 1518–1532.
[13] N. Tsuji, Y. Saito, H. Utsunomiya, S. Tanigawa, Ultra-fine grained bulk steel produced by accumulative roll-bonding (ARB) process, Scr. Mater. 40 (1999) 795–800.
[14] J.J. Sun, H. Wang, B. Xu, L. Jiang, S.W. Guo, X.J. Sun, D.W. Yu, F. Liu, Y.N. Liu, Making low-alloyed steel strong and tough by designing a dual-phase layered structure, Acta Mater 227 (2022) 117701.
[15] T. Inoue, K. Yuuji, Effect of initial notch orientation on fracture toughness in fail-safe steel, J. Mater. Sci. 48 (2013) 4766–4772.
[16] Standardization administration of china, steel and steel products—location and preparation of samples and testpieces for mechanical testing GB/T 2975-2018, State Administration for Market Regulation, Beijing, 2018.
[17] Z. Cheng, H. Zhou, Q. Lu, H. Gao, L. Lu, Extra strengthening and work hardening in gradient nanotwinned metals, Science 362 (2018) 559–567.
[18] L. Zhu, H. Ruan, A. Chen, X. Guo, J. Lu, Microstructures-based constitutive analysis for mechanical properties of gradient-nanostructured 304 stainless steels, Acta Mater 128 (2017) 375–390.
[19] X. Wu, P. Jiang, L. Chen, F. Yuan, Y.T. Zhu, Extraordinary strain hardening by gradient structure, Proc. Natl. Acad. Sci. U.S.A. 111 (2014) 7197–7201.
[20] T.H. Fang, W.L. Li, N.R. Tao, K. Lu, Revealing extraordinary intrinsic tensile plasticity in gradient nano-grained copper, Science 331 (2011) 1587–1590.
[21] Y. Lin, Q. Yu, J. Pan, F. Duan, R.O. Ritchie, Y. Li, On the impact toughness of gradient-structured metals, Acta Mater 193 (2020) 125–137.
[22] R.Q. Cao, Q. Yu, J. Pan, Y. Lin, A. Sweet, Y. Li, R.O. Ritchie, On the exceptional damage-tolerance of gradient metallic materials, Mater. Today 32 (2020) 94–107.
[23] G.V.S. Kumar, K.R. Mangipudi, G.V.S. Sastry, L.K. Singh, S. Dhanasekaran, K. Sivaprasad, Excellent combination of tensile ductility and strength due to nanotwinning and a bimodal structure in cryorolled austenitic stainless steel, Sci. Rep-UK 10 (2020) 1–9.
[24] J.X. Huang, Y. Liu, T. Xu, X.F. Chen, Q.Q. Lai, L.R. Xiao, Z.Y. Pan, B. Gao, H. Zhou, Y.T. Zhu, Dual-phase hetero-structured strategy to improve ductility of a low carbon martensitic steel, Mater. Sci. Eng. A 834 (2022) 142584.
[25] X.L. Wu, M.X. Yang, F.P. Yuan, G.L. Wu, Y.J. Wei, X.X. Huang, Y.T. Zhu, Heterogeneous lamella structure unites ultrafine-grain strength with coarse-grain ductility, Proc. Natl. Acad. Sci. 112 (2015) 14501–14505.
[26] Radhakanta Rana, Shiv Brat Singh, Automotive Steels, in: C.I. Garcia (Ed.), 6-High Strength Low Alloyed (HSLA) Steels, Woodhead Publishing, England, 2017, pp. 145–167.
[27] Z.B. Dai, H. Chen, R. Ding, Q. Lu, C. Zhang, Z.G. Yang, S. van der Zwaag, Fundamentals and application of solid-state phase transformations for advanced high strength steels containing metastable retained austenite, Mater. Sci. Eng. R 143 (2021) 100590.
[28] Z.D. Wang, B.X. Wang, B. Wang, Y. Tian, T. Zhang, G. Yuan, Z.Y. Liu, G.D. Wang, Development and application of thermo-mechanical control process involving ultra-fast cooling technology in China, ISIJ Int 59 (2019) 2131–2141.
[29] H. Mabuchi, T. Hasegawa, T. Ishikawa, Metallurgical features of steel plates with ultra fine grains in surface layers and their formation mechanism, ISIJ Int 39 (1999) 477–485.
[30] N.D. Alexopoulos, A. Stylianos, J. Campbell, Dynamic fracture toughness of Al-7Si-Mg (A357) aluminum alloy, Mech. Mater. 58 (2013) 55–68.
[31] N.D. Alexopoulos, A. Stylianos, Impact mechanical behaviour of Al-7Si-Mg (A357) cast aluminum alloy. The effect of artificial aging, Mater. Sci. Eng. 528 (2011) 6303–6312.
[32] P.R. Sreenivasan, S.L. Mannan, Dynamic J-R curves and tension-impact properties of AISI 308 stainless steel weld, Int. J. Fracture 101 (2000) 229–249.
[33] American society for testing materials, annual book of standards, ASTM, E1820-17a, Standard test method for measurement of fracture toughness, West Conshohocken, 2013, pp. 1–54.
[34] T. Kobayashi, I. Yamamoto, M. Niinomi, Introduction of a new dynamic fracture toughness evaluation system, J. Test. Eval. 21 (1993) 145–153.
[35] K. Toshiro, Y. Isamu, N. Mitsuo, Evaluation of dynamic fracture toughness parameters by instrumented Charpy impact test, Eng. Fract. Mech. 24 (1986) 773–782.
[36] P.R. Sreenivasan, S.L. Mannan, Dynamic J-R curves and tension-impact properties of AISI, Int. J. Fracture 101 (2000) 229–249.

[37] X.F. Xie, Z.M. Xie, R. Liu, Q.F. Fang, C.S. Liu, W.Z. Han, X.B. Wu, Hierarchical microstructures enabled excellent low-temperature strength-ductility synergy in bulk pure tungsten, Acta Mater 228 (2022) 117765.

[38] Z. Zhang, F.H. Shen, H.Q. Liu, Könemann Markus, Münstermann Sebastian, Temperature-dependent deformation and fracture properties of low-carbon martensitic steel in different stress states, J. Mater. Res. Technol. 25 (2023) 1931–1943.

[39] F.H. Shen, Münstermann Sebastian, J.H. Lian, A unified fracture criterion considering stress state dependent transition of failure mechanisms in bcc steels at -196 °C, Inter. J. Plast. 156 (2022) 103365.

[40] K.T. Venkateswara Rao, W.K. Yu, R.O. Ritchie, Cryogenic toughness of commercial aluminum-lithium alloys: role of delamination toughening, Metall. Trans. A 20 (1989) 485–497.

[41] L. Liu, Q. Yu, Z. Wang, J. Ell, M.X. Huang, R.O. Ritchie, Making Ultrastrong steel tough by grain-boundary delamination, Science 368 (2020) 1347–1352.

[42] R.W. Hertzberg, R.P. Vinci, J.L. Hertzberg, Deformation and fracture mechanics of engineering materials, 6th ed., John Wiley & Sons, Hoboken, 2020.

[43] D. Anderson, S. Winkler, A. Bardelcik, M.J. Worswick, Influence of stress triaxiality and strain rate on the failure behavior of a dual-phase DP780 steel, Mater. Design 60 (2014) 198–207.

[44] R.O. Ritchie, The conflicts between strength and toughness, Nat. Mater. 10 (2011) 817–822.

[45] M.E. Launey, R.O. Ritchie, On the fracture toughness of advanced materials, Adv. Mater. 21 (2009) 2103–2110.

[46] X.R. Liu, S.D. Zhang, H. Feng, J. Wang, P. Jiang, H.B. Li, F.P. Yuan, X.L. Wu, Outstanding fracture toughness combines gigapascal yield strength in an N-doped heterostructured medium-entropy alloy, Acta Mater 255 (2023) 119079.

[47] Z.X. Shang, T.Y. Sun, J. Ding, N.A. Richter, N.M. Heckman, B.C. White, B.L. Boyce, K. Hattar, H.Y. Wang, X. Zhang, Gradient nanostructured steel with superior tensile plasticity, Sci. Adv. 9 (2023) 1–12.

[48] Q.S. Pan, L.X. Zhang, R. Feng, Q.H. Lu, K. An, A.C. Chuang, J.D. Poplawsky, P.K. Liaw, L. Lu, Gradient cell–structured high-entropy alloy with exceptional strength and ductility, Science 374 (2021) 984–989.

[49] Y.T. Zhu, K. Ameyama, P.M. Anderson, I.J. Beyerlein, H.J. Gao, H.S. Kim, E. Lavernia, S. Mathaudhu, H. Mughrabi, R.O. Ritchie, N. Tsuji, X.Y. Zhang, X.L. Wu, Heterostructured materials: superior properties from hetero-zone interaction, Mater. Res. Lett. 9 (2021) 1–31.

[50] Y. Wang, G.X. Yang, W.J. Wang, X. Wang, Q. Li, Y.J. Wei, Optimal stress and deformation partition in gradient materials for better strength and tensile ductility: a numerical investigation, Sci. Rep-UK 7 (2017) 10954.

[51] J.F. Zhao, X.C. Lu, F.P. Yuan, Q.H. Kan, S.X. Qu, G.Z. Kang, X. Zhang, Multiple mechanism based constitutive modeling of gradient nanograined material, Int. J. Plast. 125 (2020) 314–330.

[52] Z. Shen, R.H. Wagoner, W.A.T. Clark, Dislocation and grain boundary interactions in metals, Acta Metall 36 (1988) 3231–3242.

[53] R. Gholizadeh, A. Shibata, N. Tsuji, Global view for grain refinement in ultra-low-C IF steel during high-strain deformation at various temperatures and strain rates, Materialia 6 (2019) 100262.

[54] S.D. Zhang, M.X. Yang, F.P. Yuan, L.L. Zhou, X.L. Wu, Extraordinary fracture toughness in nickel induced by heterogeneous grain structure, Mater. Sci. Eng. A 830 (2022) 142313.

[55] Standardization administration of China, nickel alloy steel plates for low temperature pressure vessels GB/T 24510-2017, General Administration of Quality Supervision, Inspection and Quarantine of the People's Republic of China, Beijing, 2017.

[56] J. Chen, Z.Y. Liu, G.D. Wang, Exploring the improvement of strength and cryogenic impact toughness in hot-rolled high Mn austenitic steel for cryogenic application, J. Mater. Res. Technol. 21 (2022) 3732–3745.

[57] Z.G. Liu, X.H. Gao, M. Xiong, P. Li, R.D.K. Misra, D.Y. Rao, Y.C. Wang, Role of hot rolling procedure and solution treatment process on microstructure, strength and cryogenic toughness of high manganese austenitic steel, Mater. Sci. Eng. A 807 (2021) 140881.

[58] Y.H. Nam, J.S. Park, U.B. Baek, J.Y. Suh, S.H. Ncihm, Low-temperature tensile and impact properties of hydrogen-charged high-manganese steel, Inter. J. Hydrogen Energ. 44 (2019) 7000–7013.

[59] S.S. Sohn, S. Hong, J. Lee, B.C. Suh, S.K. Kim, B.J. Lee, N.J. Kim, S. Lee, Effects of Mn and Al contents on cryogenic-temperature tensile and Charpy impact properties in four austenitic high-Mn steels, Acta Mater 100 (2015) 39–52.

[60] L.S. Li, D.Z. Yang, G.S. Wei, C.M. Wayman, Structure and properties of low-carbon high-manganese cast steels for cryogenic use, Metallography 15 (1982) 355–365.

[61] D. Zhang, G. Liu, K. Zhang, X. Sun, X. Liang, Q. Yong, Effect of Nb microalloying on microstructure evolution and mechanical properties in low carbon medium manganese steel, Mate. Sci. Eng. A 824 (2021) 141813.

[62] L. Huang, X.T. Deng, J. Liu, Z.D. Wang, Relationship between retained austenite stability and cryogenic impact toughness in 0.12 C-3.0 Mn low carbon medium manganese steel, Acta Metall. Sin. 53 (2016) 316–324.

[63] X. Xi, J. Wang, X. Li, L. Chen, Z. Wang, The role of intercritical annealing in enhancing low-temperature toughness of Fe-C-Mn-Ni-Cu structural steel, Metall. Mater. Trans. A 50 (2019) 2912–2921.

[64] M. Wang, Z.Y. Liu, Effects of ultra-fast cooling after hot rolling and intercritical treatment on microstructure and cryogenic toughness of 3.5% Ni steel, J. Mater. Eng. Perform. 26 (2017) 3016–3024.

[65] M. Wang, Z.Y. Liu, C.G. Li, Effects of ultra-fast cooling after hot rolling and lamellarizing on microstructure and cryogenic toughness of 5% Ni steel, Acta Metall. Sin. 53 (2017) 947–956.

[66] W. Hou, Q. Liu, J. Gu, Nano-sized austenite and Cu precipitates formed by using intercritical tempering plus tempering and their effect on the mechanical property in a low carbon Cu bearing 7 Ni steel, Mater. Sci. Eng. A 780 (2020) 139186.

[67] S.S.M. Tavares, C.R. Rodrigues, C.A.S. de Oliveira, C.B. Woyames, J. Dille, Influence of heat treatments on microstructure and toughness of 9% Ni steel, J. Mater. Eng. Perform. 27 (2018) 1530–1536.